Humanization of *SRGAP2C* expression increases cortico-cortical connectivity and reliability of sensory-evoked responses in the mouse brain

Ewoud R.E. Schmidt[1,3], Hanzhi T. Zhao[2,3], Elizabeth M. C. Hillman[2,3], and Franck Polleux[1,3,4 #]

[1] Department of Neuroscience

[2] Department of Biomedical Engineering and Radiology

[3] Mortimer B. Zuckerman Mind Brain Behavior Institute

[4] Kavli Institute for Brain Science, Columbia University, New York, NY 10032, USA

[#] Address correspondence to:
Franck Polleux, Ph.D.
Columbia University
Department of Neuroscience
Mortimer B. Zuckerman Mind Brain Behavior Institute
Kavli Institute for Brain Science
Jerome L. Greene Science Center
3227 Broadway
L-5-050, MC 9853
New York, NY 10027

fp2304@columbia.edu

Summary

The remarkable cognitive abilities characterizing humans has been linked to unique patterns of connectivity characterizing the neocortex. Comparative studies have shown that human cortical pyramidal neurons (PN) receive a significant increase of synaptic inputs when compared to other mammals, including non-human primates and rodents[1–4], but how this may relate to changes in cortical connectivity and function remains largely unknown. We previously identified a human-specific gene duplication (HSGD), *SRGAP2C,* that, when induced in mouse cortical PNs drives human-specific features of synaptic development, including a correlated increase in excitatory (E) and inhibitory (I) synapse density[5,6]. However, the origin and nature of this increased connectivity and its impact on cortical circuit function was unknown. Here, using a combination of transgenic approaches and quantitative monosynaptic tracing, we demonstrate that humanization of *SRGAP2C* expression in the mouse cortex leads to a specific increase in local and long-range cortico-cortical inputs received by layer 2/3 cortical PNs. Moreover, using *in vivo* 2-photon imaging in the barrel cortex of awake mice, we show that humanization of SRGAP2C expression increases the reliability and selectivity of sensory-evoked responses in layer 2/3 PNs. Our results suggest that the emergence of *SRGAP2C* during human evolution led to increased local and long-range cortico-cortical connectivity and improved reliability of sensory-evoked cortical coding.

Recent studies have led to the identification of some of the genomic mechanisms and corresponding cellular and molecular substrates underlying human brain evolution. For example, during human brain development, prolonged neurogenesis and the expansion of a specific class of neural progenitors, the outer radial glia (oRG), have been proposed to lead to higher neuronal production, in particular of supragranular layer 2/3 PNs[7–10]. However, besides the tangential expansion of the cortex, human brain evolution has critically relied on changes in neuronal connectivity[1–4,11], for which the genetic, cellular and molecular substrates remain largely unknown. We previously identified a specific HSGD affecting Slit-Robo GTPase Activating Protein 2A (*SRGAP2A*) which led to the emergence of the human-specific paralog SRGAP2C[5,6]. When expressed in mouse cortical pyramidal neurons (PNs) *in vivo*, SRGAP2C inhibits the function of

its ancestral copy *SRGAP2A* and phenocopies a partial loss of SRGAP2A function, resulting in changes in synaptic development mimicking those characterizing human cortical PNs. These include an increase in the density of both excitatory and inhibitory synapses received by layer 2/3 PNs and neotenic features of E and I synaptic development[5,6]. These findings suggest that cortical PNs expressing SRGAP2C receive increased number of synaptic inputs and are part of more densely connected circuits. However, these results raised some important questions: (1) what is the nature and the origin of these increased number of inputs? And (2) how do these SRGAP2C-induced changes in structural connectivity affect the function of cortical circuits?

To investigate these questions, we developed a novel transgenic mouse line allowing for spatial and temporal control of SRGAP2C expression by generating a *Rosa26-SRGAP2C* knock-in mouse line (SRGAP2C mice) allowing for SRGAP2C expression in a Cre-dependent manner (**Fig. 1c, d** and **Extended Data Fig. 1**). In this study, we will refer to SRGAP2C mice as animals that are heterozygous for the *Rosa26-SRGAP2C* allele, unless otherwise indicated. To determine the origin of increased connectivity received by layer 2/3 PNs following humanization of SRGAP2C expression during development, we developed a strategy using sparse *in utero* cortical electroporation (IUCE) combined with monosynaptic rabies tracing[12,13] (**Fig. 1a, b**). IUCE experiments were performed with a low amount of plasmid encoding Cre recombinase (see Methods), which led to a sparse population of layer 2/3 cortical PNs in the barrel field of the primary somatosensory cortex (bfS1) that express SRGAP2C in an otherwise wild-type brain (**Fig. 1a-g**). In addition, we co-electroporated a Cre-dependent plasmid expressing mTagBFP-HA, histone-tagged-GFP (hGFP), TVA^{66T} receptor, and N2c Glycoprotein[12,14] from a single cistron (**Fig. 1b**). TVA expression enables infection by EnvA pseudotyped G-deleted N2c rabies virus (CVS-N2c$^{\Delta G}$ [EnvA] RABV), while N2c glycoprotein facilitates trans-synaptic and retrograde spread of the virus (**Fig. 1a**). Hence, Cre-induced expression of SRGAP2C, hGFP, TVA and N2c marks a sparse population of SRGAP2C-expressing neurons and primes these 'starter' neurons for infection and trans-synaptic spread by RABV. When these animals reached adulthood (>P65),

we performed stereotactic unilateral injection of RABV into bfS1 (**Fig. 1a**). One week after infection, robust expression of tdTomato was observed in neurons located in brain regions throughout the mouse brain (**Fig. 1e-g**). A low number of layer 2/3 PNs expressing both tdTomato and nuclear hGFP were observed, indicating that initial infection by RABV was limited to a sparse number of starter neurons. Whole mouse brains were digitally reconstructed and the anatomical position of each traced neuron was mapped onto a reference atlas based on the Allen Institute Common Coordinate Framework[15] (**Fig. 2a** and **Extended Movie 1**). This allowed us to analyze each RABV traced brain within a common 3D reference space. Traced neurons were present in a large number of cortical and subcortical regions (**Extended Data Fig. 2**, n = 10 for WT and n = 7 for SRGAP2C mice). However, over 95% (95.8% ± 1.5% for WT, 96.3% ± 1% for SRGAP2C, mean ± s.e.m.) of traced neurons were localized in five distinct brain regions (**Fig. 2b-d**): ipsilateral S1, S2, M2, contralateral S1 cortex and ipsilateral thalamus.

A large fraction of the traced neurons was observed locally, surrounding the starter neuron in the ipsilateral S1 (**Fig. 2b, c** and **Extended Data Fig. 4a**). We also consistently observed traced neurons in the ipsilateral secondary motor cortex (M2), ipsilateral secondary somatosensory cortex (S2), and the primary sensory cortex contralateral to the injection site. In addition to these cortical inputs, a sizeable number of inputs originated from subcortical regions. The majority of these neurons were located in thalamic nuclei, including the ventral-anterior lateral/medial (VAL/VM), ventral posterior (VP) and posterior (PO) nuclei (**Fig. 2b-d** and **Extended Data Fig. 3**), confirming previous studies showing that layer 2/3 PNs receive direct input from these thalamic nuclei, including inputs from VAL/VM[16–18]. We next quantified the number of inputs received by layer 2/3 cortical PNs by calculating the Index of Connectivity (IOC), i.e. the number of traced neurons normalized by the number of starter neurons. Interestingly, when we assessed IOC for each brain region as a whole, we found a significant increase in SRGAP2C mice for long-range cortico-cortical projections from M2 and contralateral S1 (**Fig. 2d**, $P = 2.54 \times 10^{-2}$ for M2 and $P = 1.56 \times 10^{-2}$ for contralateral S1). This led to a specific increase in cortico-cortical inputs that

SRGAP2C-expressing layer 2/3 PNs receive without a corresponding change in subcortical inputs (**Fig. 2e**). Connectivity originating in M2 was increased equally for both supra- and infragranular layers ($P = 2.99 \times 10^{-2}$ for supragranular and $P = 4.1 \times 10^{-3}$ for infragranular), maintaining the relative proportion between supra- and infragranular inputs (**Fig. 2f-h**). In contrast, while for contralateral S1 we also observed an increase for both supra- and infragranular inputs (**Fig. 2i,** $P = 1.77 \times 10^{-2}$ for supragranular and $P = 1.39 \times 10^{-2}$ for infragranular), the increase was relatively larger for inputs originating in the infragranular layers of contralateral S1 (**Fig. 2j, k**). As a result, inputs from contralateral S1 onto *SRGAP2C* expressing layer 2/3 PNs was more balanced between supra- and infragranular layer as opposed to WT neurons for which the majority of contralateral inputs originate in supragranular layers (**Fig. 2k**). Interestingly, when we analyzed the layer-specific contribution of S2, we found a significant increase for inputs originating in layer 4 of S2 ($P = 2.63 \times 10^{-2}$), a projection that has recently been described as a non-canonical cortical feedback pathway between S2 and S1[19]. Together, our data shows that humanization of SRGAP2C expression specifically increases the number of long-range cortical inputs layer 2/3 PNs receive, without affecting the number of subcortical inputs (**Fig. 2e**). Importantly, increased connectivity was not caused by differences in cortical depth or number of starter neurons (**Extended Data Fig. 4b**). As expected, we observed a positive linear relationship between the number of infected starter neurons and the number of traced neurons. However, we found no correlation between IOC and number of starter neurons, which confirmed that our approach allows for the comparison of brains with small differences in the number of starter neurons (**Extended Data Fig. 4c, d**).

Besides long-range cortical and subcortical inputs, layer 2/3 cortical PNs in bfS1 receive a large number of inputs originating from within S1. These presynaptic neurons are located around the starter neurons (**Fig. 2c** and **Fig. 3a**) and represent the majority of inputs layer 2/3 PNs receive (**Fig. 3c**). When quantifying IOC for S1 as a whole we noticed a trend toward an increase in IOC, but this did not reach significance (**Fig. 3b**, $P = 0.109$). Local inputs onto layer 2/3 PNs consists

of excitatory inputs from other PNs and inhibitory inputs from interneurons of which the majority expresses either parvalbumin (PV) or somatostatin (SST). We wondered whether expression of SRGAP2C selectively changed the number of excitatory or inhibitory inputs layer 2/3 PNs receive since we previously demonstrated that SRGAP2C increased the density of both E and I synapses[6]. We performed post hoc immunofluorescent staining of sections from RABV traced brains for PV and SST and quantified IOC for each of these subtypes (**Fig. 3d, e**). Since PV and SST expressing interneurons provide the majority of inhibitory input onto layer 2/3 PNs we classified RABV traced cells negative for these markers as excitatory[20]. Interestingly, while the IOC or distribution of PV-positive and SST-positive cells was not different between WT and SRGAP2C expressing neurons (**Fig. 3e** and **Extended Data Fig. 5d-f**), inputs from excitatory neurons was significantly increased (**Fig. 3e**, $P = 3.3 \times 10^{-2}$).

We next examined the laminar distribution of excitatory and inhibitory (SST and PV combined) inputs and while we observed no differences for supragranular inputs, we found a layer-specific increase for excitatory inputs originating in the granular and infragranular layers (**Fig. 3f,g** and **Extended Data Fig. 5b**, $P = 6.8 \times 10^{-3}$ and $P = 4.31 \times 10^{-2}$ for excitatory neurons in the granular and infragranular layer, respectively). However, because the increase was stronger for layer 4, this layer-specific increase altered the relative contribution of inputs from each layer, with a relative increase in layer 4 inputs and a relative reduction in inputs from layer 2/3 and upper layer 5 (**Extended Data Fig. 5c**). The spatial distribution of locally traced neurons was not changed, indicating that the increased input came from the same local cluster of neurons and did not originate from more distantly located neurons (**Fig. 3f** and **Extended Data Fig. 5a**).

Connectivity in the mammalian neocortex is highly organized with neurons targeting specific layers of the cortex to selectively innervate neuronal subtypes and subcellular compartments[21,22]. The selective increase in cortico-cortical connectivity we observe in SRGAP2C-expressing layer 2/3 PNs may therefore arise from changes in synaptic density localized to specific dendritic domains. Our previous work focused on the analysis of apical oblique dendrites, but did not

examine whether SRGAP2C expression affects synaptic development in other dendritic compartments[5,6]. To extend these findings in our newly developed SRGAP2C mouse line, we used the same IUCE approach used for monosynaptic rabies tracing by electroporating a Cre-dependent plasmid encoding mTagBFP-HA (**Fig. 1b**) together with low amounts of Cre recombinase encoding plasmid, in heterozygous SRGAP2C or wild-type (WT) control mice. Electroporating low levels of Cre led to sparse labeling of layer 2/3 PNs in bfS1 (**Fig. Extended Data Fig. 6a, b**), allowing reliable quantification of dendritic spine density along distal tuft, apical oblique, and basal dendritic segments in optically-isolated neurons (**Extended Data Fig. 6**). While spine density was increased in the apical oblique and distal tuft segment of adult *SRGAP2C*-expressing neurons, no such increase was observed for basal dendrites (**Extended Data Fig. 6c**, $P = 1.92 \times 10^{-2}$ for distal, $P = 1.5 \times 10^{-3}$ for apical oblique, $P = 3.01 \times 10^{-1}$ for basal). Spine size was similar between WT and SRGAP2C animals, showing that synapses are mature in SRGAP2C-expressing neurons after P65 (**Extended Data Fig. 7a**) as previously reported[5,6]. Interestingly, we observed a strong correlation in spine density between apical oblique and basal dendrites (**Extended Data Fig. 7b**), but this correlation was reduced in SRGAP2C expressing neurons.

Local and long-range cortico-cortical connections play a critical role in the hierarchical processing of sensory information and response properties of layer 2/3 PNs[23,24]. Selectively increasing cortico-cortical connectivity may therefore directly modify how layer 2/3 PNs process sensory information. To test this, we performed *in vivo* 2-photon Ca^{2+} imaging in WT and SRGAP2C mice crossed with Thy1-GCaMP6f and Nex^{Cre} mice ($n = 4$ WT and $n = 3$ SRGAP2C mice). This enabled us to image neuronal activity in layer 2/3 PNs ($n = 962$ neurons for WT and $n = 618$ for SRGAP2C) and ensured that all imaged PNs express SRGAP2C. Whisker stimulation (see Methods and **Extended Data Fig. 8a**) was performed for 5 seconds per trial (repeated 24 times separated by 25 seconds inter-trial interval per imaging session), leading to neuronal responses that were either time-locked to the onset of the stimulus (ON), responses that occurred during progression of the

stimulus, or responses time-locked to the offset of the stimulus (OFF) (**Fig. 4a-e**). Transients that were not time-locked to the onset of the stimulus but did occur during the 5 second stimulus window often had longer response durations compared to ON or OFF responses (**Fig. 4d**). We therefore refer to these as plateau responses. Overall, we observed no difference between WT and SRGAP2C mice regarding the fraction of layer 2/3 PNs that responded to the stimulus either as ON, OFF or plateau responders (**Extended Data Fig. 8b**). We next measured the response probability for each neuron by calculating the fraction of trials that led to a response (ON or OFF), excluding neurons for which no responses were observed for any trials. Similar to previous studies[25–27], overall sensory-evoked response probabilities were low in WT layer 2/3 PNs, with a long-tail distribution towards a small group of neurons that responded with high probability (**Extended Data Fig. 8c**). Interestingly, SRGAP2C expressing neurons had a higher response probability specifically for responses time-locked to the onset of the stimulus, while a small but significant reduction in response probability was observed for plateau responses (**Fig. 4f-h**, $P = 6.4 \times 10^{-3}$ for ON, $P = 3.21 \times 10^{-1}$ for OFF, and $P = 4.31 \times 10^{-2}$ for Plateau). In addition, the duration of plateau responses was significantly longer in SRGAP2C mice ($P < 0.0001$), with a number of responses spanning nearly the entire stimulus (**Fig. 4i-k**). Each whisker stimulus was separated by an inter-trial interval (ITI) of 25 seconds. Activity during the ITI was significantly reduced for SRGAP2C neurons for both the number of transients and transient amplitude (**Fig. 4l**, median number of transients: 1.25 for WT and 0.5 for SRGAP2C, median transient amplitude: 1.26 for WT and 1.05 for SRGAP2C), which was not explained by differences in behavioral activity, such as whisking or grooming (**Extended Data Fig. 8d**). Together with a higher response probability for the onset of the stimulus, this led to activity patterns that were more restricted to stimulus epochs, resulting in an increase in response selectivity of SRGAP2C expressing layer 2/3 PNs (**Fig. 4m**).

Discussion

In summary, our results demonstrate that expression of the human-specific gene duplication SRGAP2C alters cortical circuit architecture by increasing the number of local and long-range cortical inputs onto layer 2/3 PNs, and improves their coding properties in response to sensory stimulation (**Extended Data Fig. 9**). Our results reveal that changes in synaptic development regulated by SRGAP2C can cell-autonomously shape the structural organization of cortical circuits, and indicates that (1) the wiring principles governing connectivity in the mammalian neocortex are in part regulated by synapse availability on the postsynaptic side and (2) that changes in the relative contribution of cortico-cortical connectivity is a substrate of the genomic process shaping human brain evolution. It has previously been suggested that synapse availability is regulated by both synaptic density and spine neck length[28], two features that are increased in mouse cortical PNs when SRGAP2C is expressed[5]. Increasing these features specifically for excitatory inputs located on apical dendrites, which are the main recipients of cortico-cortical inputs[29,30], is compatible with our main finding showing that SRGAP2C selectively increases cortico-cortical connectivity received by layer 2/3 PNs.

In contrast to increased number of presynaptic neurons providing excitatory inputs to layer 2/3 PNs, we observed no difference in the number of presynaptic PV or SST neurons in neurons expressing SRGAP2C. This is surprising in light of our previous work, which showed that excitatory and inhibitory synapse density is increased to a remarkably similar level upon humanization of SRGAP2C in layer 2/3 PNs[6]. Our current results may hint at two types of connectivity changes in SRGAP2C mice: an increase in excitatory synapses that recruits inputs from a larger number of presynaptic neurons, while an increase in the number of inhibitory synapses may lead to increased input from the same number of axons from inhibitory neurons, potentially through increased branching. This model is supported by previous studies showing that, in response to changes in neuronal activity in excitatory neurons, interneurons regulate the number of inhibitory synaptic inputs through changes in axon branching[31,32].

By increasing cortico-cortical connectivity from deeper cortical layers as well as long-range feedback projections from more distant cortical regions (S2, M2, and contralateral S1), SRGAP2C expression selectively increases excitatory cortical feedforward and feedback inputs received by layer 2/3 PNs. Integration of these feedforward and feedback inputs is critical for information processing in the cortex. For example, top-down inputs from cortical areas such as M2 onto S1 PNs play a critical role in sensory processing, motor learning, and memory[33–35]. One mechanism through which these feedback cortico-cortical inputs control sensory processing is by altering response reliability of cortical neurons in primary sensory areas such as S1[36,37]. Furthermore, local feedforward inputs, such as from layer 4, play an important role in driving layer 2/3 PNs in response to sensory input. Layer 4 is one of the main thalamo-recipient layers and relays sensory input to both superficial and deep layers of the cortex. However, while these inputs are numerous (between 300 to 400 layer 4 spiny neurons converge onto a single layer 2/3 PN[38]), modeling the impact of these connections has suggested that the majority of layer 4 inputs would be unable to drive spike firing in layer 2/3 PNs, and that driving responses of layer 2/3 PNs relies on strong inputs from a small number of neurons[39,40]. Increasing the number of layer 4 neurons that input onto layer 2/3 PNs may increase the probability that such strong inputs occur, and consequently increase the probability of layer 2/3 PN firing in response to whisker stimulation. While the precise function of many of these local and long-range cortico-cortical inputs still needs to be explored, it has become clear that feedforward and feedback inputs can dynamically modify how cortical neurons respond to sensory input by, among other features, changing their response reliability[41]. The specific increase in feedforward and feedback cortico-cortical connectivity we observed in humanized SRGAP2C mice presents a likely explanation for the increased response reliability of layer 2/3 PNs to sensory stimuli. It is worth noting that we did not observe increased local recurrent, or horizontal, connectivity among layer 2/3 PNs. Recruitment of local horizontal connectivity, while increasing activity in other layers, leads to inhibition within the layer itself, most likely through supralinear recruitment of inhibitory neurons[42–44]. Recruiting the same number of

layer 2/3 PNs in response to whisker stimulation and maintaining similar horizontal connectivity could therefore provide further opportunity for feedforward and feedback cortical inputs to increase response reliability in the primary sensory cortex.

We also observed reduced ITI activity of layer 2/3 PNs, making their responses more selective for sensory stimulation. Reduced ITI activity may be explained by increased inhibitory drive, although our previous work has shown that the magnitude of the increased synaptic density induced by SRGAP2C expression is equal for excitatory and inhibitory synapses, suggesting E/I balance is preserved[6]. However, the combination of increased response probability and sustained activity during the stimulus, together with reduced ITI activity, may suggest that the increase in excitatory synapse density in SRGAP2C expressing neurons leads to a simultaneous, maybe homeostatic, reduction in their synaptic strength. When excitatory drive is low, such as in the absence of a sensory stimulus, this would lead to a reduction in spontaneous firing rates. However, upon sensory stimulation, increased local and long-range cortical inputs may be sufficient to overcome this reduction in synapse strength and therefore more reliably recruit layer 2/3 PNs upon sensory stimulation.

The total number of layer 2/3 PNs and corresponding cortico-cortical connectivity has expanded significantly in the human brain compared to non-human primates and other mammals[11]. Our findings may offer an explanation of how human-specific modifiers of synaptic development such as SRGAP2C played a role in driving human brain evolution. Local and long-range cortico-cortical connections facilitate communication and integration of information across different functional regions of the neocortex. As such, they play an essential role in both the hierarchical processing of information, which is critical for transformation of sensory information and feature detection, as well as building predictive models of the external environment that enables the brain to make inferences about the nature of sensory inputs and relate these to appropriate behavioral responses[23,45]. Future investigations will therefore have to explore how SRGAP2C, as well as

other HSGDs, modify synaptic development, dendritic integration, and the organization of cortico-cortical connectivity, and how these changes impact overall cortical circuit function and behavior.

Acknowledgements

The transgenic inducible knockin mouse model described here was developed in collaboration with genOway (Lyon, France). We thank Thomas Reardon and Samaher Fageiry for kindly providing RABV. We thank Darcy Peterka, Miyako Hirabayashi and Qiaolian Liu for excellent technical help. We thank members of the Polleux lab and Randy Bruno for valuable discussions and inputs. This works was supported by NIH (RO1NS067557) (FP), an Award for the Roger De Spoelberch Foundation (FP), Netherlands Organization for Scientific Research (NWO Rubicon 825.14.017) (ERES), the European Molecular Biology Organization (EMBO Long-Term Fellowship ALTF 1055-2014) (ERES) and NINDS K99 (K99 NS109323-01) (ERES).

Methods

Mice

All animals were handled according to protocols approved by the institutional animal care and use committee (IACUC) at Columbia University, New York. All mice used in experiments were adults (>P65), heterozygous for indicated transgenes, and were maintained on a 12h light/dark cycle. Nex^{Cre} ($NeuroD6^{tm1(cre)Kan}$) mice[46] were obtained through Jax and induce recombination in dorsal telencephalic-derived postmitotic neurons giving rise to all pyramidal neurons throughout the cortex, hippocampus and amygdala but not in astrocytes, interneurons or microglial cells in these structures. Thy1-GCaMP6f mice[47] were obtained through Jax (C57BL/6J-Tg(Thy1-GCaMP6f)GP5.17Dkim/J) and stochastically express GCaMP6f in a subset of excitatory pyramidal neurons in various brain regions, including cortex and hippocampus.

Conditional SRGAP2C expressing mice were generated using homologous recombination in C57BL/6J mouse ES cells (see **Extended Data Fig. 1** for details) in collaboration with genOway (France). A targeting vector containing a CAG promoter, *SRGAP2C*-3xHA cDNA, rabbit-globin poly-A, a floxed STOP-neomycin cassette, and homology arms consisting of sequences between exon 1 and exon 2 of the *Rosa26* locus was constructed. In addition, Diptheria Toxin A (DTA) cDNA was placed downstream of the 3' homology arm for negative selection of non-recombined ES cell clones. Southern blot analysis was used to confirm homologous recombination of the targeting vector in ES cell clones. Recombined ES cell clones were injected into C57BL/6J blastocysts and re-implanted into OF1 pseudo-pregnant females to generate chimeric males. Male chimeras were subsequently bred with wild-type C57BL/6J females to generate an F1 population of SRGAP2C mice. Heterozygous mice ($Rosa26^{SRGAP2C}$(F/+)) were confirmed carriers of the transgene by genomic PCR and Southern blot analysis (**Extended Data Fig. 1**). Wild-type and SRGAP2C alleles are identified with PCR of genomic DNA using the following primers: 5'-CAATACCTTTCTGGGAGTTCT-3' and 5'-CTGCATAAAACCCCAGATGAC-3' for detection of the WT allele, and 5'-CATGGGGGATATGGCTTCC-3' and 5'-GGAACATCGTATGGGTAAGCG-3' for detecting the presence of *Rosa26* targeted SRGAP2C. For *in utero* electroporation experiments, mice were crossed once with the outbred strain 129S2/SvPasCrl mice (obtained from Charles River) to produce F1 hybrids females used to generate timed-pregnant females by crossing with $Rosa26^{SRGAP2C}$(F/+) heterozygous males (on pure C57BL/6J). This strategy is used because pure C57BL/6J females often cannibalize their offspring at birth following *in utero* electroporation experiments but not these F1 (C57BL/6J; 129S2/SvPasCrl) females.

Western Blot

Cre-dependent expression of SRGAP2C-HA protein was analyzed by crossing SRGAP2C mice with Nex-Cre mice[46] to induce expression of SRGAP2C in all excitatory forebrain neurons. Cortical hemispheres were dissected and homogenized in ice-cold homogenization buffer (N-PER Neuronal Protein Extraction Reagent (ThermoFisher Scientific) with cOmplete Protease Inhibitor Cocktail (Roche), 10 μM MG-132 (Sigma-Aldrich), and Benzonase (EMD Millipore)) using a disposable Biomasher II (Kimble Chase). After homogenization, samples were incubated for 30 min at 4°C in homogenization buffer and subsequently centrifuged at 10,000 g for 30 min in a cooling centrifuge at 4°C. Samples were prepared in Laemmli buffer (Bio-Rad) containing 10% 2-Mercaptoethanol and boiled at 95°C for 5 min. Using SDS-PAGE, proteins were separated and then transferred to a polyvinylidene difluoride (PVDF) membrane (Immobilon-FL, EMD Millipore). Western blotting was performed using anti-HA primary (1:1000, Anti-HA.11, Biolegend) and anti-actin (1:5000, MAB1501, Millipore) together with goat-anti-mouse IgG conjugated to IRDye 800CW (1:10,000, Li-Cor) and goat-anti-mouse IgG conjugated to IRDye 680RD (1:40,000). Imaging of immunoblots was performed on an Odyssey CLx Imaging System (Li-Cor).

DNA constructs

The BHTG construct was generated by subcloning mTagBFP-3xHA, histone-GFP, TVA66T and the N2c glycoprotein together with 2A self-cleaving peptide sequences (see **Fig. 1b** for details) in between NheI and AscI cloning sites of the pAAV-Ef1a-DIO eNpHR 3.0-EYFP plasmid (Addgene plasmid # 26966) using Gibson assembly cloning. pCAG-Cre was generated in the Polleux lab, as previously described[48].

***In utero* cortical electroporation**

In utero cortical electroporation (IUCE) was performed at E15.5 on isoflurane anaesthetized timed-pregnant SRGAP2C or control female mice as previously described[49], with the following modifications. Endotoxin-free DNA containing 1μg/μl of BHTG plasmid and 10-20 ng/μl Cre

plasmid was injected into the ventricles of E15.5 embryos using a heat-pulled capillary. Electroporation was performed by applying 5 pulses of 42 V for 50 ms with 500 ms intervals using a 3 mm diameter platinum tweezer electrode (Nepa Gene) and a square wave electroporator (ECM 830, BTX). After placing embryos back into the abdominal cavity, the incision was closed using sutures and the mouse allowed to recover on a heating plate.

Virus injection

Adult mice were anaesthetized using isoflurane and placed in a stereotactic frame (Stoelting). A small burr hole was drilled over the barrel field of the primary sensory cortex (1.3 mm posterior and 3 mm lateral to Bregma[50]) using a high-speed dental drill. A glass pipette (Drummond Scientific) was heat-pulled (Narishige PC-10) to produce a tip of approximately 10 µm in diameter. It was then filled with viral vector solution containing CVS-N2c$^{\Delta g}$ [EnvA] RABV-tdTomato and lowered into the brain to a depth of 200-300 µm. Virus was subsequently injected at bouts of 25 nl at 2 nl/s with a 20s interval until a total volume of 400-500 nl was injected. The glass injection pipette was left for 2 min after the injection was completed after which it was slowly removed. The skin was closed using sutures and the mouse was allowed to recover on a heating plate. Mice were left for 7 days to allow enough time for RABV-tdTomato to reach sufficient levels of expression in both starter neurons and presynaptic inputs.

Reconstruction of rabies traced brains

Tissue preparation. After 7 days of RABV tracing, mice were anaesthetized with isoflurane and intracardiac perfusion was performed using 4% paraformaldehyde (Electron Microscopy Sciences) in PBS. Brains were isolated and incubated overnight in a 4% paraformaldehyde in PBS solution at 4°C. The following day, brains were washed in PBS and sectioned along the coronal plane at 100 µm using a vibrating microtome (Leica VT1200S). Approximately 100 sections were collecting spanning the most rostral part of the cortex to the cerebellum. Sections

were stained using Hoechst 33258 (Sigma-Aldrich) and subsequently mounted on glass slides in Fluoromount-G aqueous mounting medium (ThermoFisher Scientific).

Imaging. Sections were first imaged on a Nikon SMZ18 stereo microscope with automatic stage using a SHR Plan Apo 1X at a zoom magnification of 4x. Stitching was performed directly after imaging using Nikon NIS-Elements software. Sections containing both tdTomato and hGFP positive cells were subsequently imaged by collecting Z-stacks on a Nikon A1 confocal microscope using a 10x Plan Apo NA 0.45 objective (Nikon) for identification of RABV starter neurons, which we identified by co-expression of hGFP and tdTomato. Additional confirmation of starter neurons was done by imaging these neurons again using a 40x Plan Apo NA 0.95 (Nikon) objective.

Section alignment and registration to atlas. Imaged sections were aligned using rigid body alignment in StackReg (ImageJ plugin) and when necessary manual adjustments were made using Adobe Photoshop. Neurons were subsequently counted and annotated using Cell Counter (ImageJ plugin) after which sections and coordinates were imported into 3ds Max (Autodesk). Landmarks were then manually placed at multiple anatomical locations (113 anatomical landmarks) corresponding to landmarks we assigned to a 3D mouse brain atlas imported from the Allen Brain Institute (Common Coordinate Framework 3). Landmarks were placed at anatomical regions easily identified in imaged sections, such as the first section containing hippocampus or the first section where the corpus callosum forms a continuous bundle. In addition, a single landmark indicating the point at which both cortical hemispheres meet was assigned to each section (designated as midline landmark). Using these assigned landmarks, together with custom-written scripts in MAXScript, the 1) section stack was resized to match the reference brain size, 2) based on the midline landmark each section was aligned along the dorsal/ventral axis of the reference brain, and 3) using anatomical landmarks each neuron was assigned to the corresponding location in the reference brain. Finally, in order to assign proper cortical depth to each neuron, the pial surface was traced and reconstructed for each section and

the distance to the pial surface for each neuron was measured along the line that intersects the pial surface perpendicularly. Neurons were color coded according to their assigned brain region or their calculated cortical depth to manually confirm proper alignment to the reference brain. Finally, the 3D position and assigned brain region for each neuron was exported for subsequent analysis.

Immunohistochemistry

Dendritic spine analysis. Tissue sections were washed in PBS and subsequently blocked for 3 h at room temperature in blocking buffer (PBS containing 0.2% Triton X-100 (Sigma-Aldrich) and 5% goat serum (Gibco)). Next, sections were incubated with primary antibody in PBS containing 0.2% Triton-X100 and 5% goat serum overnight at 4°C. The next day, sections were washed 3x for 30 min in PBS containing 0.2% Triton-X100. Sections were then incubated for 1 h using with secondary antibodies conjugated to Alex Fluor-546 or 647 of appropriate species (1:500, ThermoFisher Scientific). After several washes in PBS sections were mounted on glass slides using Fluoromount-G. Imaging of dendritic spines was performed using a Nikon A1 confocal microscope. First, low magnification Z-stack images were collected using a 20x Plan Apo NA 0.75 objective (Nikon) to visualize the entire dendritic tree of optically isolated neurons. Next, appropriate terminal branches were selected for distal, apical oblique, and basal dendritic segments, for which we collected Z-stack images using a 100x H-TIRF, NA 1.49 objective (Nikon).
Identification of interneurons. Tissue sections were washed in PBS and subsequently blocked overnight at 4°C in blocking buffer (PBS containing 1% Triton X-100 (Sigma-Aldrich) and 5% goat serum (Gibco)). The following day, sections were washed 3x for 1 h in PBS containing 0.5% Triton-X100. Next, sections were incubated with primary antibody in PBS containing 0.5% Triton-X100 and 0.5% goat serum for 4 days at 4°C. Sections were then washed 3x 1 h in PBS containing 0.5% Triton-X100 after which they were incubated with secondary antibodies conjugated to Alex Fluor-488, 546, and 647 of appropriate species (1:500, ThermoFisher Scientific). After several

washes in PBS sections were mounted on glass slides and mounted in Fluoromount-G. Z-stacks were collected by imaging on a Nikon A1 confocal microscope using a 10x Plan Apo NA 0.45 objective (Nikon) to identify neuronal identity for Rabv-traced neurons. Primary antibodies used were mouse anti-HA (1:1000, Anti-HA.11, Biolegend), rat anti-somatostatin (1:100, MAB354, Millipore), guinea pig anti-parvalbumin (1:200, 195004, Synaptic Systems), and rabbit anti-DsRed (1:500, 632496, Takara Bio).

Two-photon calcium imaging

Adult mice were anaesthetized using isoflurane and injected with buprenorphine (0.1 mg/kg body weight), after which the dorsal skull was exposed and cleaned with a razor blade. A craniotomy was performed and a glass window was placed over the barrel field of the primary sensory cortex. The window was glued in place using cyanoacrylate glue, after which a custom head plate was secured onto the skull using both cyanoacrylate glue and dental acrylic cement. Mice were allowed to recover for a minimum of 7 days, after which imaging in awake mice (*n*=4 WT and *n*=3 SRGAP2C) was conducted on a Bergamo II two-photon microscope (Thorlabs) running Scanimage, using a 16x 0.8 NA objective (Nikon) and 920-nm wavelength Ti-Sapphire laser (Coherent). Imaging was performed 150 – 250 μm below the pial surface at 30 Hz and 512 x 512 pixels covering 830 μm x 830 μm. For whisker stimulation trials a transparent acrylic rod was placed next to the right whisker pad at a fixed distance of 2 mm. Every stimulus trial consisted of a 10 seconds pre-stimulus, 5 second stimulus, and 15 second post-stimulus period. Whisker stimuli were applied by vibrating the bar at 25Hz, a speed of more than 100 mm/s, and an amplitude of over 1 mm. To identify the responding region in the barrel field of primary sensory cortex contralateral to the stimulated whisker pad, we first performed a wide-field imaging experiment in which the entire region under the cranial window was imaged during multiple stimulus trials. The hemodynamic component was calculated and the neural signal was isolated, as previously described[51]. Subsequent two-photon imaging was performed of 2 to 3 non-

overlapping fields of view per mouse within the center of the activated area. Activity of the animal during imaging was monitored using an infrared webcam.

Data analysis

Rabies tracing. Index of connectivity (IOC) was calculated for each animal by dividing the number of traced neurons by the number of starter neurons. Average IOC density maps showing the distribution of traced neurons across the brain were generated in MATLAB (Mathworks) by generating IOC density maps per animal and subsequently combining these maps to calculate an average IOC density map per genotype. For density maps showing distribution of neurons relative to their closest starter neuron, we determined, per animal, the closest starter neuron for each traced neuron in the primary sensory cortex (S1). We then calculated the relative medial-lateral and rostro-caudal position of each traced neuron with respect to the closest starter neuron. The majority of traced neurons in S1 form a dense cloud closely around the starter neuron. However, this approach may misclassify which starter neuron belongs to which traced neurons when multiple starter neurons are in close proximity of each other. Differences in the distance between starter neurons in a single brain for WT and SRGAP2C mice could therefore obscure a potential change in the distribution of traced neurons between WT and SRGAP2C mice. We therefore analyzed the minimum distance between starter neurons for brains with more than 1 starter neurons. We found no difference in the distribution of starter neurons between WT and SRGAP2C mice (distance from starter neuron to nearest other starter neuron: 300.4 µm ± 55.92 for WT and 357.1 µm ± 74.19 for SRGAP2C, mean ± sem). Furthermore, when we analyzed brains with only 1 starter neuron (n = 3 for WT and n = 2 SRGAP2C) we similarly did not observe a change in the spatial distribution of traced neurons (data not shown).

Dendritic spines. Nikon NIS-Elements was used to generate a z-stack maximum intensity projection of selected dendritic branches. We then quantified spine density and head size by

tracing the dendritic segment to measure the dendritic length and drawing ROIs around the spine head as visualized by the mTagBFP-HA filler signal.

Two-photon image processing and analysis. Non-rigid motion correction of acquired images was performed using NoRMCorre, as previously described[52]. Regions of interest (ROIs) were manually drawn over soma of individual neurons. All subsequent analyses were done using custom-written MATLAB code, which is available upon request. Time-courses were calculated as the mean of all pixels within the ROI. Neuropil signal was estimated by dilating neuronal ROIs by 4 pixels to form a ring-shaped neuropil ROI around the soma of each neuron. To remove neuropil contamination, we subtracted the ΔF/F neuropil signal from the ΔF/F neuronal signal. To avoid subtraction of signal not considered neuropil contamination, we excluded pixels in the neuropil ROI that contained transients exceeding two times the standard deviation of the difference between the neuropil and neuronal signals, as previously described[53]. To identify the response type per stimulus for each neuron, we aligned all time-courses to their respective stimulus onset and performed K-means clustering with 60 clusters and correlation as the distance metric. Common time-courses were identified by running K-means 200 times with random initialization. The resulting outputs of the repeated K-means were clustered a final time to obtain a set of representative responses. Clusters with responses where the onset time was time-locked with the start or end of the whisker stimulus were determined to be an on- or off-type response, respectively. Those occurring during the duration of stimulus were grouped as plateau-type responses. Neuronal responses were subsequently assigned to a cluster by evaluating the Pearson's correlation between the time-course and each basis time-course. The highest correlation value greater than 0.4 was determined to be the representative time-course. Duration of plateau responses were calculated as the time where z-scored plateau-type time-courses were greater than 1. To characterize activity during the inter-trial interval (ITI), transients were identified by finding the local maxima during ITI periods. Peaks were constrained to having widths of at least two frames, a minimum ΔF/F of 0.5, and a relative increase in ΔF/F of 6 times the standard

deviation compared to the preceding local minimum. A frame-to-frame sliding window correlation analysis of webcam images was done to determine periods and duration of active behavior, such as whisking or grooming.

Statistics

Statistical analysis was performed using Prism 6 (Graphpad Software). Normality was checked using Kolmogorov-Smirnov test. A non-parametric test (Kruskal-Wallis with post-hoc Dunn's multiple comparison test or Mann-Whitney U test) was used when distribution deviated significantly from normality. A test was considered significant when $p < 0.05$. For RABV tracing, 10 WT and 7 *SRGAP2C* mice were obtained from a minimum of four independent litters. For *in vivo* spine analysis, data was obtained from at least six animals from a minimum of three independent litters. For two-photon microscopy experiments 4 WT and 3 SRGAP2C mice were obtained from two independent litters. Independent data points shown denote data from individual animals.

References

1. Seeman, S. C. *et al.* Sparse recurrent excitatory connectivity in the microcircuit of the adult mouse and human cortex. *Elife* **7**, 292706 (2018).
2. Mohan, H. *et al.* Dendritic and axonal architecture of individual pyramidal neurons across layers of adult human neocortex. *Cereb. Cortex* **25**, 4839–4853 (2015).
3. Benavides-Piccione, R., Ballesteros-Yáñez, I., DeFelipe, J. & Yuste, R. Cortical area and species differences in dendritic spine morphology. *J. Neurocytol.* **31**, 337–46 (2003).
4. Elston, G. N., Benavides-Piccione, R. & DeFelipe, J. The pyramidal cell in cognition: a comparative study in human and monkey. *J. Neurosci.* **21**, RC163 (2001).
5. Charrier, C. *et al.* Inhibition of SRGAP2 function by its human-specific paralogs induces neoteny during spine maturation. *Cell* **149**, 923–35 (2012).
6. Fossati, M. *et al.* SRGAP2 and Its Human-Specific Paralog Co-Regulate the Development of Excitatory and Inhibitory Synapses. *Neuron* **91**, 356–369 (2016).
7. Hansen, D. V, Lui, J. H., Parker, P. R. L. & Kriegstein, A. R. Neurogenic radial glia in the outer subventricular zone of human neocortex. *Nature* **464**, 554–561 (2010).
8. Florio, M. *et al.* Human-specific gene ARHGAP11B promotes basal progenitor amplification and neocortex expansion. *Science* **347**, 1465–1470 (2015).
9. Fiddes, I. T. *et al.* Human-Specific NOTCH2NL Genes Affect Notch Signaling and Cortical Neurogenesis. *Cell* **173**, 1356-1369.e22 (2018).
10. Suzuki, I. K. *et al.* Human-Specific NOTCH2NL Genes Expand Cortical Neurogenesis through Delta/Notch Regulation. *Cell* **173**, 1370-1384.e16 (2018).
11. Buckner, R. L. & Krienen, F. M. The evolution of distributed association networks in the human brain. *Trends Cogn. Sci.* **17**, 648–65 (2013).
12. Reardon, T. R. R. *et al.* Rabies Virus CVS-N2cΔG Strain Enhances Retrograde Synaptic Transfer and Neuronal Viability. *Neuron* **89**, 1–14 (2016).
13. Wickersham, I. R., Finke, S., Conzelmann, K. K. & Callaway, E. M. Retrograde neuronal

tracing with a deletion-mutant rabies virus. *Nat. Methods* **4**, 47–49 (2007).

14. Miyamichi, K. *et al.* Dissecting local circuits: parvalbumin interneurons underlie broad feedback control of olfactory bulb output. *Neuron* **80**, 1232–45 (2013).
15. Allen Institute for Brain Science. Allen Mouse Common Coordinate Framework. *Technical White Paper* 1–18 (2015).
16. DeNardo, L. a, Berns, D. S., DeLoach, K. & Luo, L. Connectivity of mouse somatosensory and prefrontal cortex examined with trans-synaptic tracing. *Nat. Neurosci.* 1–13 (2015). doi:10.1038/nn.4131
17. Viaene, A. N., Petrof, I. & Sherman, S. M. Synaptic Properties of Thalamic Input to Layers 2/3 and 4 of Primary Somatosensory and Auditory Cortices. *J. Neurophysiol.* **105**, 279–292 (2010).
18. Zhang, S. *et al.* Organization of long-range inputs and outputs of frontal cortex for top-down control. *Nat. Neurosci.* **19**, (2016).
19. Minamisawa, G., Kwon, S. E., Chevée, M., Brown, S. P. & O'Connor, D. H. A Non-canonical Feedback Circuit for Rapid Interactions between Somatosensory Cortices. *Cell Rep.* **23**, 2718-2731.e6 (2018).
20. Tremblay, R., Lee, S. & Rudy, B. GABAergic Interneurons in the Neocortex: From Cellular Properties to Circuits. *Neuron* **91**, 260–292 (2016).
21. Harris, K. D. & Shepherd, G. M. G. The neocortical circuit: themes and variations. *Nat. Neurosci.* **18**, 170–181 (2015).
22. Douglas, R. J. & Martin, K. A. C. C. Neuronal circuits of the neocortex. *Annu. Rev. Neurosci.* **27**, 419–51 (2004).
23. Adesnik, H. & Naka, A. Cracking the Function of Layers in the Sensory Cortex. *Neuron* **100**, 1028–1043 (2018).
24. Petersen, C. C. H. & Crochet, S. Synaptic Computation and Sensory Processing in Neocortical Layer 2/3. *Neuron* **78**, 28–48 (2013).

25. Clancy, K. B., Schnepel, P., Rao, A. T. & Feldman, D. E. Structure of a Single Whisker Representation in Layer 2 of Mouse Somatosensory Cortex. *J. Neurosci.* **35**, 3946–3958 (2015).

26. De Kock, C. P. J., Bruno, R. M., Spors, H. & Sakmann, B. Layer- and cell-type-specific suprathreshold stimulus representation in rat primary somatosensory cortex. *J. Physiol.* **581**, 139–154 (2007).

27. Sato, T. R., Gray, N. W., Mainen, Z. F. & Svoboda, K. The functional microarchitecture of the mouse barrel cortex. *PLoS Biol.* **5**, 1440–1452 (2007).

28. Stepanyants, A., Hof, P. R. & Chklovskii, D. B. Geometry and structural plasticity of synaptic connectivity. *Neuron* **34**, 275–288 (2002).

29. Shipp, S. Structure and function of the cerebral cortex. *Curr. Biol.* **17**, R443-9 (2007).

30. Thomson, A. M. & Bannister, A. P. Interlaminar connections in the neocortex. *Cereb. Cortex* **13**, 5–14 (2003).

31. Chen, J. L. *et al.* Structural basis for the role of inhibition in facilitating adult brain plasticity. *Nat. Neurosci.* **14**, 587–596 (2011).

32. Pieraut, S. *et al.* Experience-dependent remodeling of basket cell networks in the dentate gyrus. *Neuron* **84**, 107–122 (2014).

33. Manita, S. *et al.* A Top-Down Cortical Circuit for Accurate Sensory Perception. *Neuron* **86**, 1304–1316 (2015).

34. Makino, H. *et al.* Transformation of Cortex-wide Emergent Properties during Motor Learning. *Neuron* **94**, 880-890.e8 (2017).

35. Gilad, A., Gallero-Salas, Y., Groos, D. & Helmchen, F. Behavioral Strategy Determines Frontal or Posterior Location of Short-Term Memory in Neocortex. *Neuron* **0**, 814-828.e7 (2018).

36. Lee, S., Carvell, G. E. & Simons, D. J. Motor modulation of afferent somatosensory circuits. *Nat. Neurosci.* **11**, 1430–1438 (2008).

37. Zagha, E., Casale, A. E., Sachdev, R. N. S., McGinley, M. J. & McCormick, D. A. Motor cortex feedback influences sensory processing by modulating network state. *Neuron* (2013). doi:10.1016/j.neuron.2013.06.008

38. Lubke, J. Morphometric Analysis of the Columnar Innervation Domain of Neurons Connecting Layer 4 and Layer 2/3 of Juvenile Rat Barrel Cortex. *Cereb. Cortex* **13**, 1051–1063 (2003).

39. Sarid, L., Bruno, R., Sakmann, B., Segev, I. & Feldmeyer, D. Modeling a layer 4-to-layer 2/3 module of a single column in rat neocortex: Interweaving in vitro and in vivo experimental observations. *Proc. Natl. Acad. Sci. U. S. A.* **104**, 16353–16358 (2007).

40. Lefort, S., Tomm, C., Floyd Sarria, J.-C. & Petersen, C. C. H. The Excitatory Neuronal Network of the C2 Barrel Column in Mouse Primary Somatosensory Cortex. *Neuron* **61**, 301–316 (2009).

41. Larkum, M. A cellular mechanism for cortical associations: An organizing principle for the cerebral cortex. *Trends Neurosci.* **36**, 141–151 (2013).

42. Adesnik, H. & Scanziani, M. Lateral competition for cortical space by layer-specific horizontal circuits. *Nature* **464**, 1155–1160 (2010).

43. Adesnik, H. Layer-specific excitation/inhibition balances during neuronal synchronization in the visual cortex. *J. Physiol.* **596**, 1639–1657 (2018).

44. Kapfer, C., Glickfeld, L. L., Atallah, B. V. & Scanziani, M. Supralinear increase of recurrent inhibition during sparse activity in the somatosensory cortex. *Nat. Neurosci.* **10**, 743–753 (2007).

45. Gilbert, C. D. & Li, W. Top-down influences on visual processing. *Nat. Rev. Neurosci.* **14**, 350–363 (2013).

46. Goebbels, S. *et al.* Genetic targeting of principal neurons in neocortex and hippocampus of NEX-Cre mice. *Genesis* **44**, 611–621 (2006).

47. Dana, H. *et al.* Thy1-GCaMP6 Transgenic Mice for Neuronal Population Imaging In Vivo.

PLoS One **9**, e108697 (2014).

48. Courchet, J. *et al.* Terminal Axon Branching Is Regulated by the LKB1-NUAK1 Kinase Pathway via Presynaptic Mitochondrial Capture. *Cell* **153**, 1510–1525 (2013).

49. Hand, R. & Polleux, F. Neurogenin2 regulates the initial axon guidance of cortical pyramidal neurons projecting medially to the corpus callosum. *Neural Dev.* **6**, 30 (2011).

50. Paxinos, G. & Franklin, K. B. J. *The mouse brain in stereotaxic coordinates*. (Academic Press, 1997).

51. Ma, Y. *et al.* Wide-field optical mapping of neural activity and brain haemodynamics: considerations and novel approaches. *Philos. Trans. R. Soc. B Biol. Sci.* **371**, 20150360 (2016).

52. Pnevmatikakis, E. A. & Giovannucci, A. NoRMCorre: An online algorithm for piecewise rigid motion correction of calcium imaging data. *J. Neurosci. Methods* **291**, 83–94 (2017).

53. Peters, A. J., Chen, S. X. & Komiyama, T. Emergence of reproducible spatiotemporal activity during motor learning. *Nature* **510**, 263–267 (2014).

Figure Legends

Fig. 1. Monosynaptic rabies tracing from a sparse population of layer 2/3 cortical pyramidal neurons.

a, **b**, Generation and subsequent tracing from SRGAP2C expressing starter neurons using rabies monosynaptic tracing. **a**, The BHTG construct (see **b**), together with Cre recombinase, is targeted to layer 2/3 cortical pyramidal neurons in the primary sensory cortex (S1) by *in utero* electroporation (IUCE) at E15.5. When mice reach adulthood (>P65), stereotactic injection of RABV leads to initial infection of starter neurons expressing the BHTG construct (1), after which it spreads to presynaptically connected neurons (2). **b**, BHTG and Cre constructs. **c-e**, Design strategy for generating SRGAP2C conditional knock in mice. **c**, 3x HA tagged *SRGAP2C* was inserted into a *Rosa26* targeting vector, which contains a CAG promoter, a floxed STOP-Neomycin cassette, and *Rosa26* homology arms. Image not to scale. **d**, Using homologous recombination, the targeting vector was inserted between exon 1 and 2 of the *Rosa26* locus. **e-g**, Coronal section of a RABV traced mouse brain with identification of starter neuron and RABV traced neurons mapped onto the Allen Reference Atlas. **e**, Coronal section stained for Hoechst (green) showing location of a starter neuron (indicated by dashed white box) in the barrel field of the primary sensory cortex (S1). Scale bar, 1 mm. **f**, Higher magnification of dashed white box area in **e**. Starter neuron (indicated by white arrow) is identified by expression of histone-GFP (hGFP, white). RABV infection is identified by expression of tdTomato (magenta). Rounded boxes indicate barrels in layer 4. Scale bar, 200 μm. **g**, High magnification of starter neuron. Scale bar, 25 μm.

Fig. 2. SRGAP2C expression increases long-range cortico-cortical connectivity

a, Reference brain (top) based on Allen Reference Atlas. Digital reconstruction of RABV traced brain and registration onto reference brain. Black arrow indicates location of starter neurons in barrel field of S1. **b**, Density plots showing distribution of traced neurons in WT and SRGAP2C

mice. Colors in density plot indicate index of connectivity (IOC): number of traced neurons / number of starter neurons). **c**, **d**, Anatomical location and quantification of RABV traced neurons. **c**, Boxes indicate location of the majority of RABV traced neurons. RABV traced neurons are located in the primary somatosensory cortex (S1) ipsilateral to the RABV injection site, secondary motor cortex (M2), secondary somatosensory cortex (S2), the primary somatosensory cortex contralateral to the injection site (Cl), and the thalamus (Th). For the thalamus, RABV traced neurons were located in the ventralanteriorlateral/medial (VAL/VM), ventral posterior (VP) and posterior (PO) subnuclei. Green arrowhead in S1 indicates RABV infected starter neuron. White arrowheads mark non-infected, electroporated neurons. White arrows mark RABV traced neurons. Roman numbers identify cortical layers. Scale bar, 500 µm. **d**, IOC for brain regions in **c**, relative to control. **e**, IOC (top) and fraction of inputs (bottom) for all RABV traced long-range inputs. Increased connectivity in SRGAP2C is selective for cortio-cortical (CC) inputs, but does not affect subcortical inputs (SC). **f-h**, IOC for supra- and infragranular layers in M2. Top left: distribution of traced neurons in WT and SRGAP2C, colors indicate IOC. Top right: IOC for supra- and infragranular layers. Bottom: distribution of traced neurons as a function or their cortical depth (left: IOC, right: fraction of total). **i-k**, same as in **f-h** for S1 contralateral to RABV injection site. Bar graphs plotted as mean ± s.e.m. Open circles in bar graphs indicate data from individual mice. **P* < 0.05, ***P* < 0.01.

Fig. 3. Expression of SRGAP2C leads to layer-specific increase in local connectivity

a-c, Index of connectivity (IOC, number of traced neurons / starter neurons) for the primary somatosensory cortex (S1). **a**, Distribution of traced neurons in WT and SRGAP2C, colors indicate IOC. **b**, IOC for primary somatosensory cortex (S1). **c**, IOC (left) and fraction (right) for all RABV traced inputs, including local cortical inputs originating in S1. Increased connectivity in SRGAP2C is selective for cortio-cortical (CC) inputs but does not affect subcortical (SC) inputs. **d**, Double immunohistochemistry of the same RABV traced brain section for Parvalbumin (top)

and Somatostatin (bottom). Bottom panels represent higher magnification of area indicated by dashed boxes, showing co-labeling of Parvalbumin and Somatostatin with RABV-tdTomato. Scale bar large panel, 200 μm. Scale bar small panel, 20 μm. **e**, IOC for excitatory, Parvalbumin (PV)-positive, and Somatostatin(SST)-positive RABV traced neurons in S1. **f**, Density plots showing distribution of traced excitatory neurons relative to their closest starter neuron for coronal (left, L and M indicate lateral and medial orientation, respectively) and sagittal view (right, R and C indicate rostral and caudal orientation, respectively). Center bins aligned with relative position of starter neuron are indicated by red dashed lines. S, supragranular, G, granular, I, infragranular layers. For coronal, bin size = 50x50 μm. For sagittal, bin size = 50x100 μm. Colors in density plots indicate IOC. **g**, IOC for excitatory neurons in supragranular, granular, and infragranular layers of S1. Open circles in bar graphs indicate individual mice. Bar graph plotted as mean ± s.e.m. *$P < 0.05$, **$P < 0.01$.

Fig. 4. SRGAP2C increases response reliability and selectivity to sensory input

a-c, Schematic of experimental approach. **d,** Singe-trial example responses. Shaded area indicates whisker stimulation. **e**, Single-trial responses of responding neurons converted to Z-scores and aligned to peak activity. **f-h**, Left panels: average calcium traces (ΔF/F) for responses time-locked to the onset of the whisker stimulus (ON), during progression of the stimulus (Plateau), or time-locked to the offset of stimulus (OFF). Shaded area indicates s.e.m. Right panels: response probability expressed as fraction of stimuli leading to a response. **i-k**, Duration of responses during plateau phase. **i**, Ten percent of single-trial plateau phase responses with longest sustained activity converted to Z-scores and sorted by duration of response. **j**, Calcium traces (ΔF/F) of bottom 15 responses shown in **i**. **k**, Cumulative probability distribution of plateau response durations (time that z-score was greater than 1). **l**, Cumulative probability distribution of transient number and amplitude during intertrial interval (ITI). **m**, Z-scored example traces

showing activity during six consecutive stimuli (shaded) and corresponding ITIs. *$P < 0.05$, **$P < 0.01$, ****$P < 0.0001$.

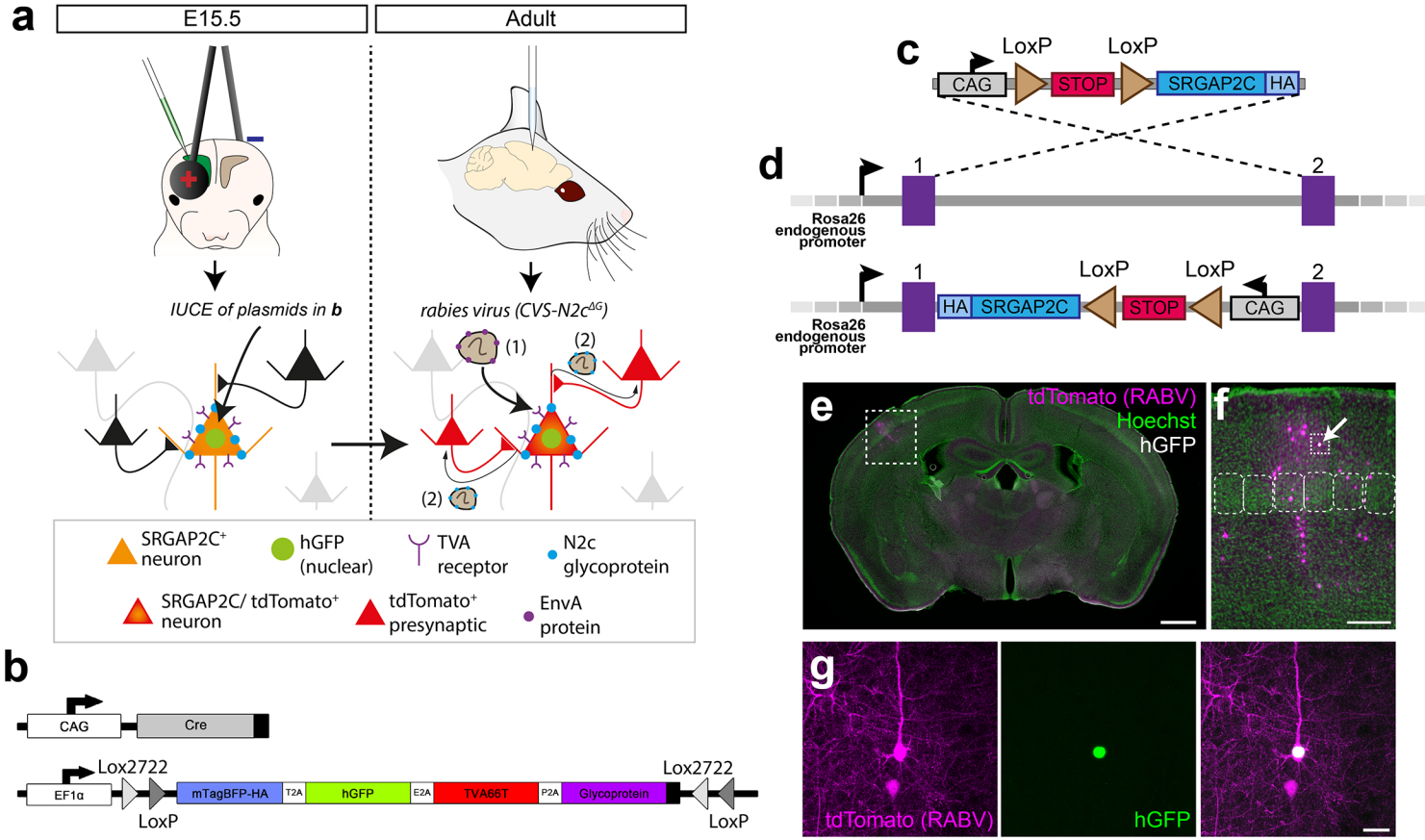
a
E15.5
Adult
IUCE of plasmids in b
rabies virus (CVS-N2c^ΔG)
(1)
(2)
(2)
SRGAP2C+ neuron
hGFP (nuclear)
TVA receptor
N2c glycoprotein
SRGAP2C/ tdTomato+ neuron
tdTomato+ presynaptic
EnvA protein
b
CAG
Cre
Lox2722
EF1α
mTagBFP-HA
T2A
hGFP
E2A
TVA66T
P2A
Glycoprotein
Lox2722
LoxP
LoxP
c
LoxP
LoxP
CAG
STOP
SRGAP2C
HA
d
1
2
Rosa26 endogenous promoter
1
LoxP
LoxP
2
HA
SRGAP2C
STOP
CAG
Rosa26 endogenous promoter
e
tdTomato (RABV)
Hoechst
hGFP
f
g
tdTomato (RABV)
hGFP

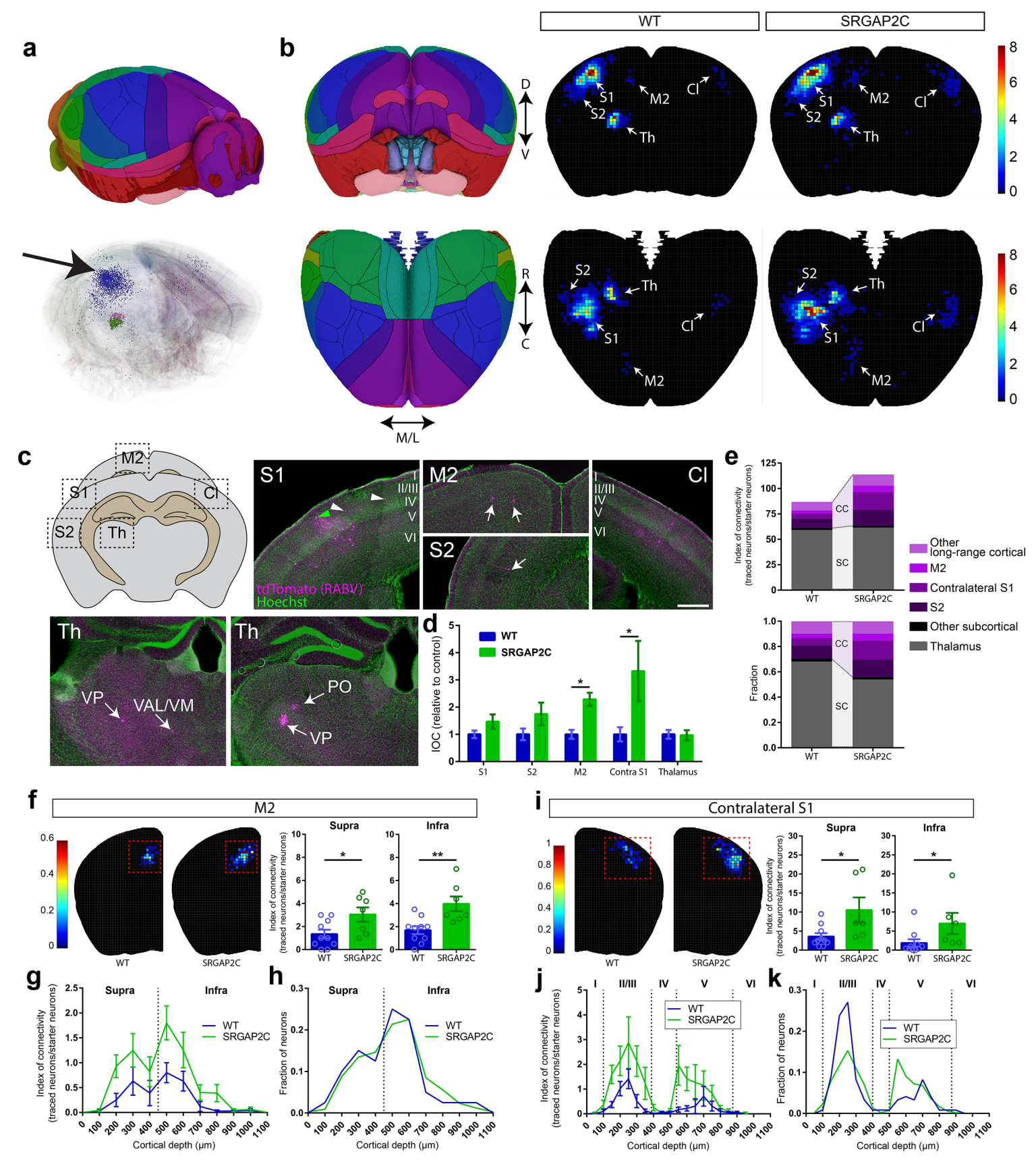
WT
SRGAP2C
a
b
D
V
R
C
M/L
S1
S2
M2
Cl
Th
c
tdTomato (RABV)
Hoechst
I
II/III
IV
V
VI
VP
VAL/VM
PO
d
WT
SRGAP2C
IOC (relative to control)
Contra S1
Thalamus
e
Index of connectivity (traced neurons/starter neurons)
CC
SC
Other long-range cortical
Contralateral S1
Other subcortical
Fraction
f
M2
Supra
Infra
i
Contralateral S1
g
h
j
k
Cortical depth (μm)
Fraction of neurons

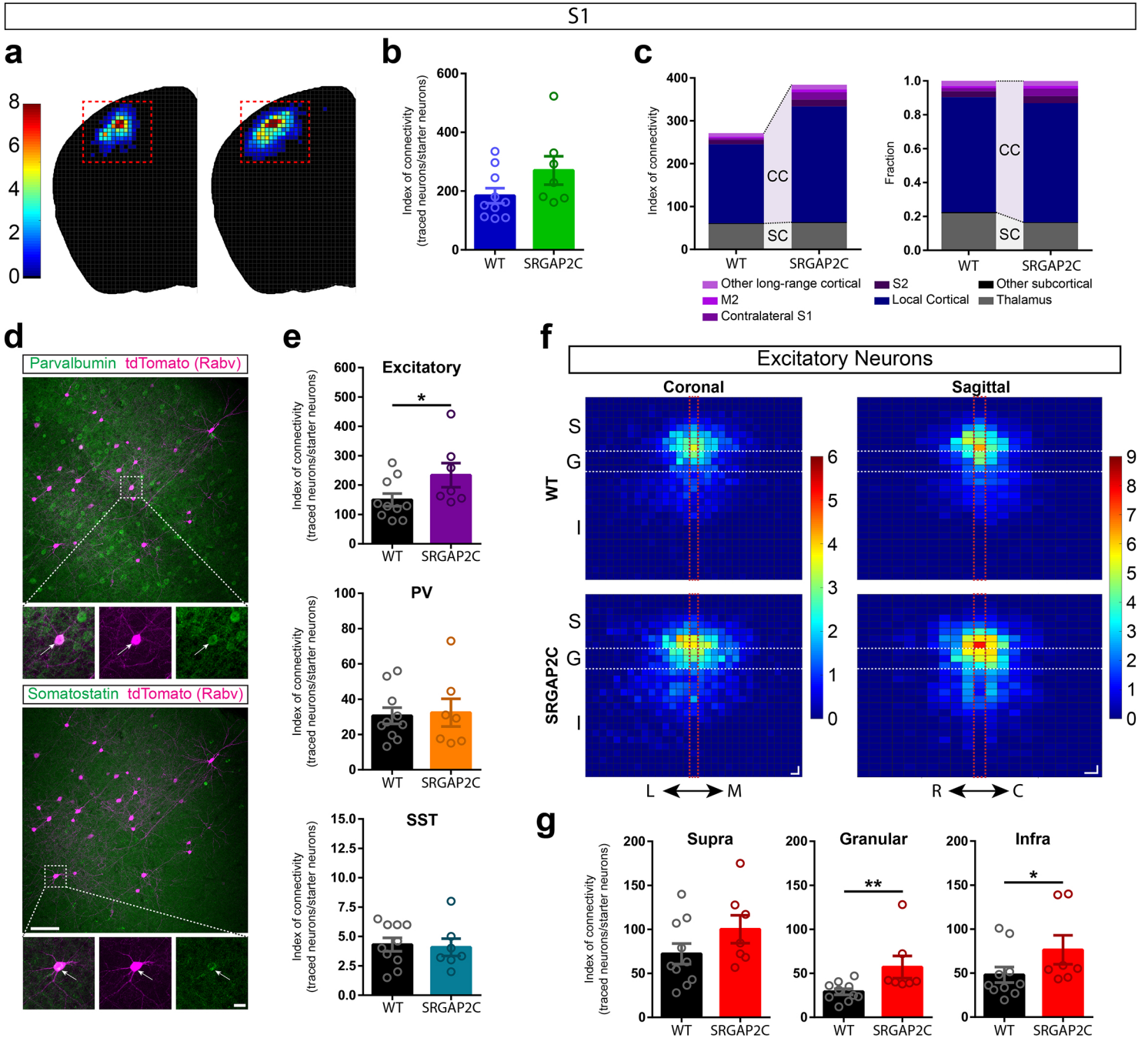
S1
a
8
6
4
2
0
b
Index of connectivity
(traced neurons/starter neurons)
600
400
200
0
WT
SRGAP2C
c
Index of connectivity
400
300
200
100
0
CC
SC
WT
SRGAP2C
Fraction
1.0
0.8
0.6
0.4
0.2
0.0
CC
SC
WT
SRGAP2C
Other long-range cortical
M2
Contralateral S1
S2
Local Cortical
Other subcortical
Thalamus
d
Parvalbumin tdTomato (Rabv)
Somatostatin tdTomato (Rabv)
e
Excitatory
*
Index of connectivity
(traced neurons/starter neurons)
600
500
400
300
200
100
0
WT
SRGAP2C
PV
Index of connectivity
(traced neurons/starter neurons)
100
80
60
40
20
0
WT
SRGAP2C
SST
Index of connectivity
(traced neurons/starter neurons)
15.0
12.5
10.0
7.5
5.0
2.5
0.0
WT
SRGAP2C
f
Excitatory Neurons
Coronal
Sagittal
WT
SRGAP2C
S
G
I
6
5
4
3
2
1
0
9
8
7
6
5
4
3
2
1
0
L
M
R
C
g
Index of connectivity
(traced neurons/starter neurons)
Supra
Granular
Infra
**
*
200
150
100
50
0
WT
SRGAP2C

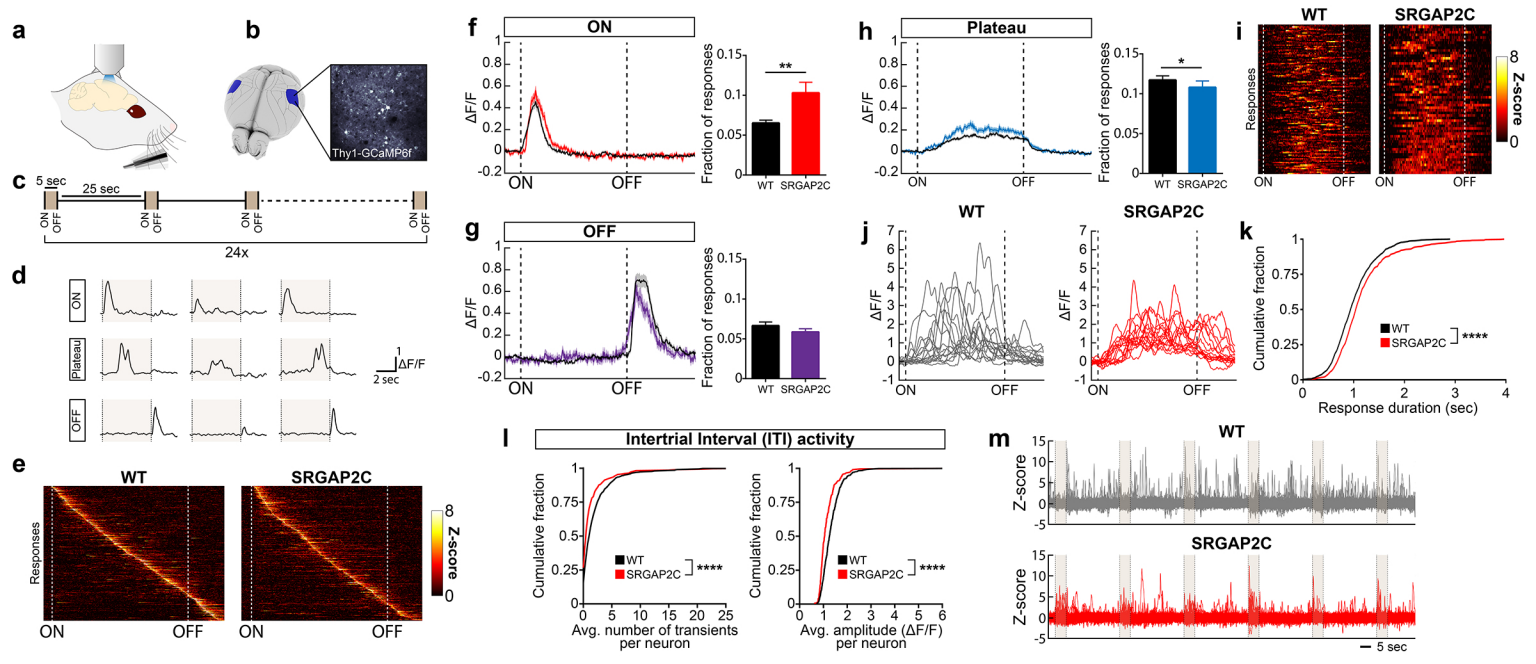
a
b
Thy1-GCaMP6f
c
5 sec
25 sec
ON
OFF
24x
d
ON
Plateau
OFF
1
ΔF/F
2 sec
e
WT
SRGAP2C
Responses
ON
OFF
8
Z-score
0
f
ON
ΔF/F
Fraction of responses
**
WT
SRGAP2C
g
OFF
h
Plateau
*
i
WT
SRGAP2C
Responses
Z-score
j
k
Cumulative fraction
Response duration (sec)
****
l
Intertrial Interval (ITI) activity
Avg. number of transients per neuron
Avg. amplitude (ΔF/F) per neuron
m
Z-score
5 sec

Supplementary Figures

Humanization of *SRGAP2C* expression increases cortico-cortical connectivity and reliability of sensory-evoked responses in the mouse brain

Ewoud R.E. Schmidt[1,3], Hanzhi T. Zhao[2,3], Elizabeth M. C. Hillman[2,3], and Franck Polleux[1,3,4 #]

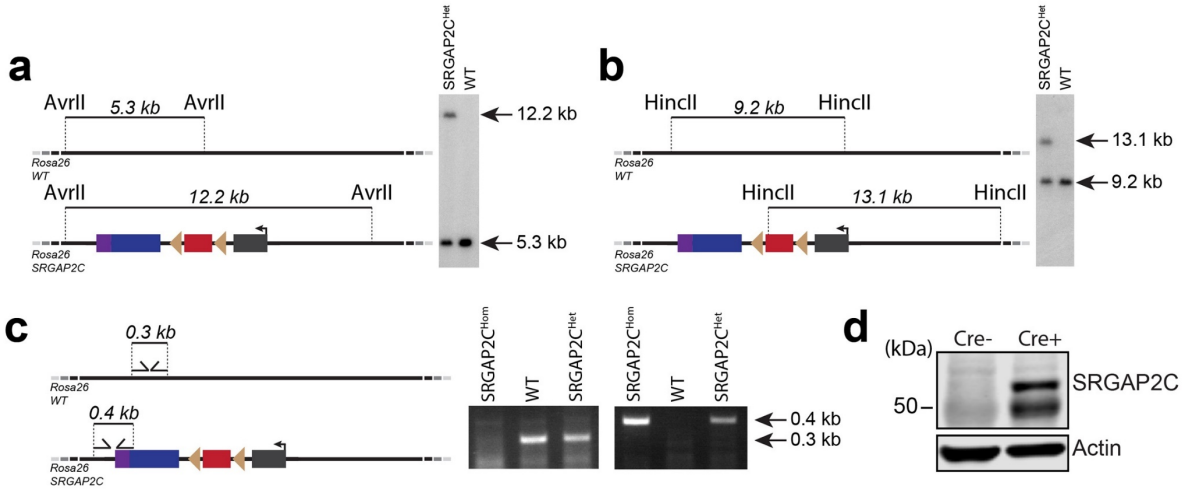

Extended Data Fig. 1. Generation of an inducible, humanized SRGAP2C transgenic mouse line.

Southern blot and genomic PCR analysis of *Rosa26* targeted SRGAP2C mice (see Methods section for details). **a**, **b**, Verification of SRGAP2C targeting in mouse embryonic stem cells using Southern blot analysis with probes that distinguish the targeted allele (12.2 kb in **a**, 13.1 kb in **b**) from the wild-type allele (5.3 kb in **a**, 9.2 kb in **b**). **c**, Mice were genotyped by genomic PCR using the forward and reverse primers indicated that distinguish the WT Rosa26 allele or the SRGAP2C allele. **d**, Western blot probed with anti-HA antibody of adult (P30) cortex isolated from SRGAP2C heterozygous conditional knock-in mice crossed with heterozygous $Nex^{Cre/+}$ mice (Cre+) or wild-type littermate (Cre-). The presence of Cre induces SRGAP2C-HA expression. Without Cre, no SRGAP2C was detected. Anti-Actin antibody was used as loading control.

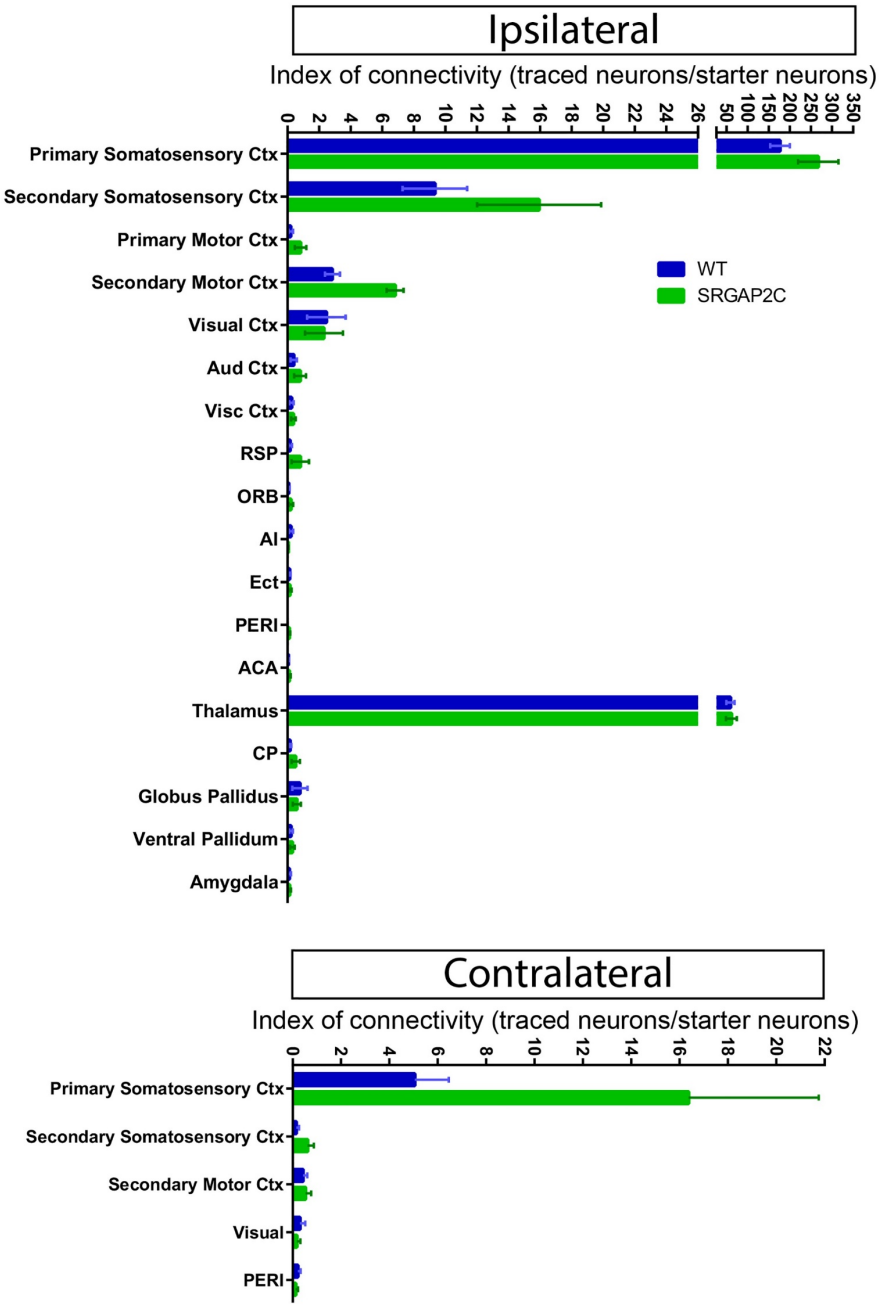

Extended Data Fig. 2. Brain regions containing RABV traced neurons

Index of connectivity (IOC, number of traced neurons / starter neurons) for brain regions ipsilateral and contralateral to the injection site. RSP, retrosplenial area, ORB, Orbital cortex, Ai, Agranular Insular cortex, Ect, Ectorhinal cortex, PERI, Perirhinal cortex, ACA, Anterior Cingulate cortex, CP, Caudate-putamen. Bar graphs plotted as mean ± s.e.m.

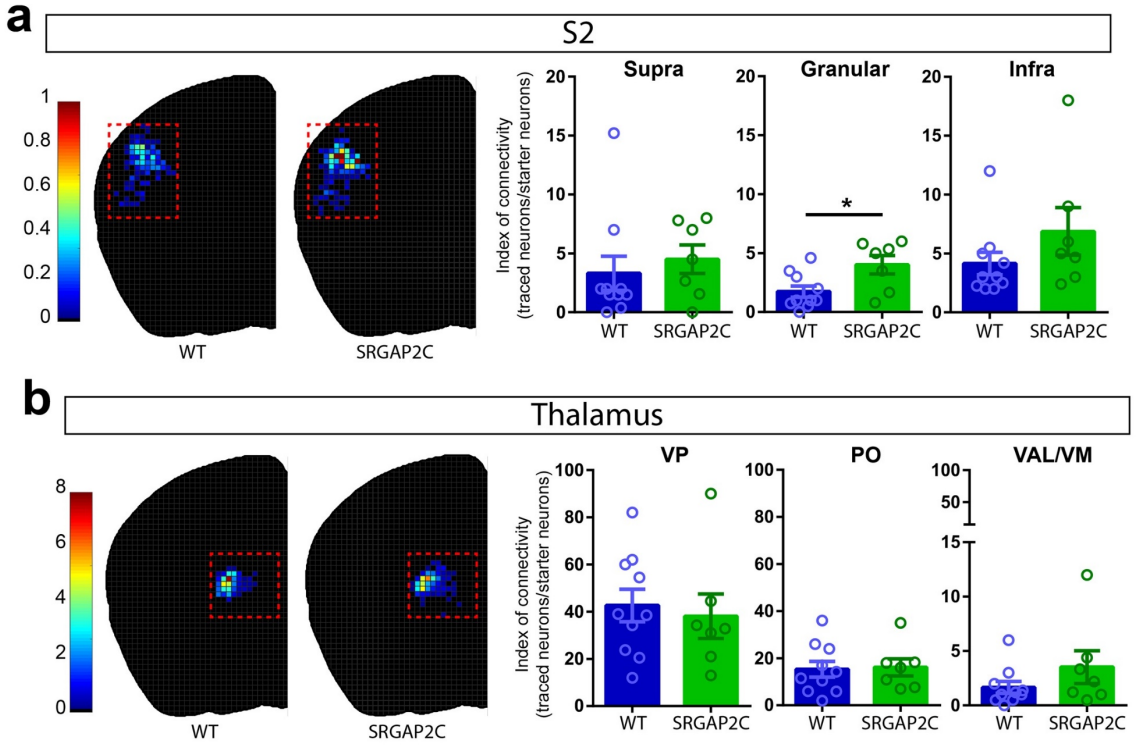

Extended Data Fig. 3. Distribution of RABV traced neurons in S2 and Thalamus

a, **b**, Index of connectivity (IOC, number of traced neurons / number of starter neurons) for secondary sensory cortex (S2) and the thalamus. **a**, IOC for traced neurons in S2. Left: distribution of traced neurons in WT and SRGAP2C, colors indicate IOC. Right: IOC for supragranular, granular and infragranular layers. **b**, Same as in **a** for Ventralanteriorlateral/medial (VAL/VM), Ventralposterior (VP), and Posterior (PO) thalamic subnuclei. Bar graphs plotted as mean ± s.e.m. Open circles in bar graphs indicate individual mice. *$P < 0.05$.

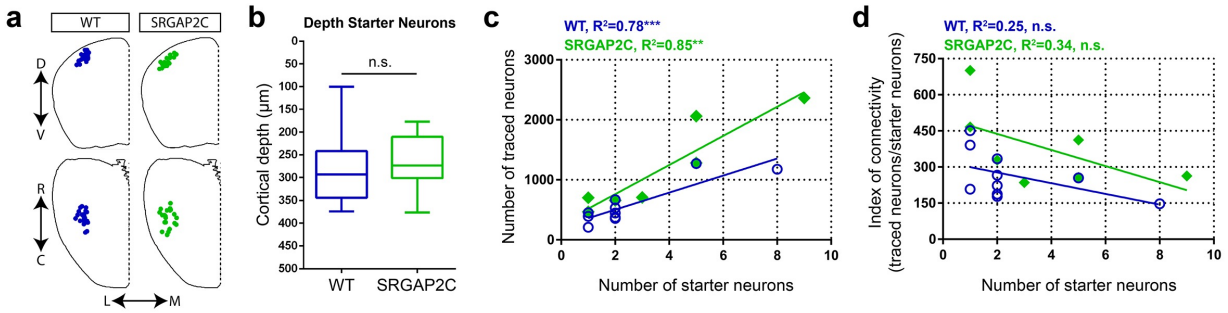

Extended Data Fig. 4. Connectivity changes are not caused by differences in cortical depth or number of starter neurons

a, Location of starter neurons (*n* = 26 starter neurons, 10 mice for WT, and *n* = 26 starter neurons, 7 mice for SRGAP2C). **b**, Cortical depth of starter neurons measured as distance from pial surface is not different between WT and SRGAP2C mice. Data shown as box-and-whisker plots. Center line indicates median, box edges represents first and third quartiles, and whiskers represent minimum and maximum values. **c**, Correlation between number of RABV infected starter neurons and RABV traced neurons (Pearson's correlation coefficient $r = 0.88$, $P = 7 \times 10^{-4}$ for WT, and $r = 0.92$, $P = 3.2 \times 10^{-3}$ for SRGAP2C). **d**, No correlation was observed between IOC and number of RABV infected starter neurons per brain (Pearson's correlation coefficient $r = -0.5$, $P = 0.14$ for WT, and $r = -0.58$, $P = 0.17$ for SRGAP2C).

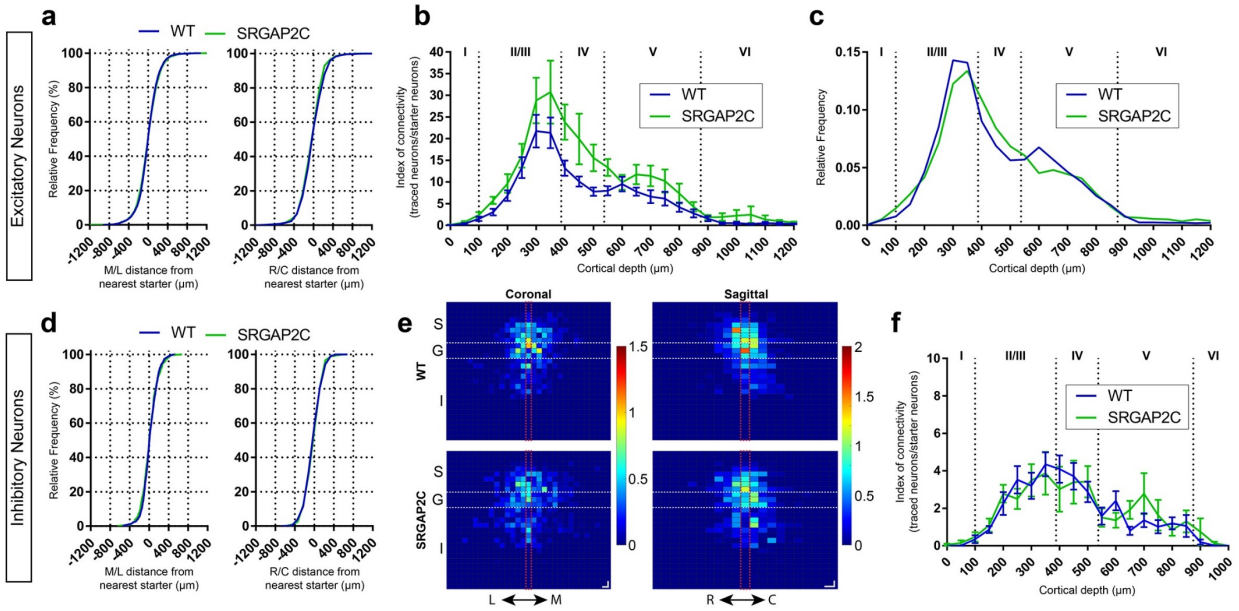

Extended Data Fig. 5. Distribution of RABV traced neurons locally in S1

a-c, Distribution of RABV traced excitatory neurons in the primary somatosensory cortex (S1). **a**, Distance between RABV traced excitatory neurons in S1 and their closest starter neuron along the medial/lateral (M/L) or rostral/caudal (R/C) plane. No difference was observed between WT and SRGAP2C mice. Data shown as relative frequency distribution. **b**, Cortical layer distribution of RABV traced excitatory neurons in S1 shown as Index of connectivity (IOC, number of traced neurons / number of starter neurons). **c**, Fraction of RABV traced neurons across cortical layers in S1. Dashed lines indicates borders between layers. Roman numericals identify cortical layers. **d-f**, Distribution of RABV traced inhibitory neurons in the primary somatosensory cortex (S1). For analysis of interneurons, Parvalbumin-positive and Somatostatin-positive were grouped together. **d**, Same as **a**, for inhibitory neurons. **e**, Density plot showing distribution of traced inhibitory neurons relative to their closest starter neuron for coronal (left, L and M indicate lateral and medial orientation, respectively) and sagittal view (right, R and C indicate rostral and caudal orientation, respectively). Center bins aligned with relative position of starter neuron are indicated by red dashed lines. S, supragranular (layer 2/3), G, granular (layer 4), I, infragranular layers (layer 5/6). For coronal, bin size = 50x50 µm. For sagittal, bin size = 50x100 µm. Colors in density plots indicate IOC. **f**, Same as in **b**, for inhibitory neurons.

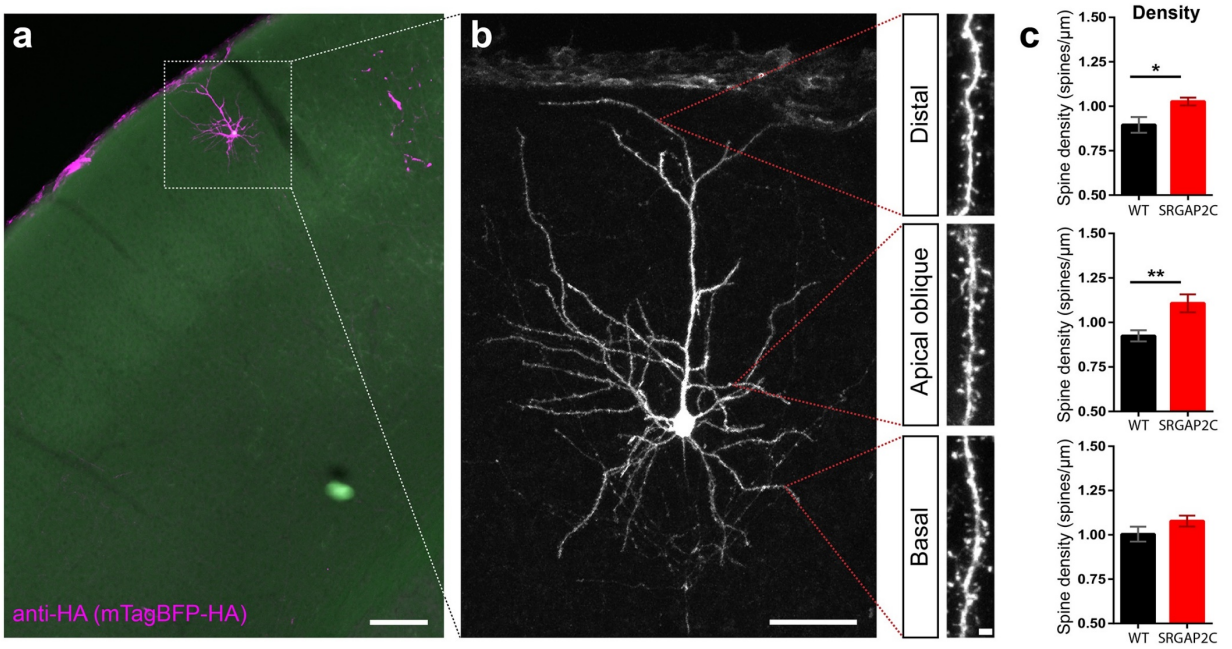

Extended Data Fig. 6. SRGAP2C expression increases synaptic density in apical dendrites

a, Coronal section stained for HA showing sparse labeling of a layer 2/3 cortical pyramidal neuron in the barrel field of the primary somatosensory cortex. Scale bar, 150 µm. **b**, Higher magnification of neuron in **a**. Red dotted lines indicate approximate location where spine density and size were quantified for distal, apical oblique, and basal dendritic compartments. Panels on right show high magnification images of dendritic segments on which spines can clearly be identified. Left panel scale bar, 50 µm. Right panel scale bar, 2 µm. **c**, Spine density is increased for apical but not basal dendritic segments. (distal: n = 21 segments for WT and SRGAP2C, apical oblique: n = 33 segments for WT and n = 24 segments for SRGAP2C, basal: n = 32 segments for WT and n = 24 segments for SRGAP2C). Bar graph plotted as mean ± s.e.m. *P < 0.05, **P < 0.01.

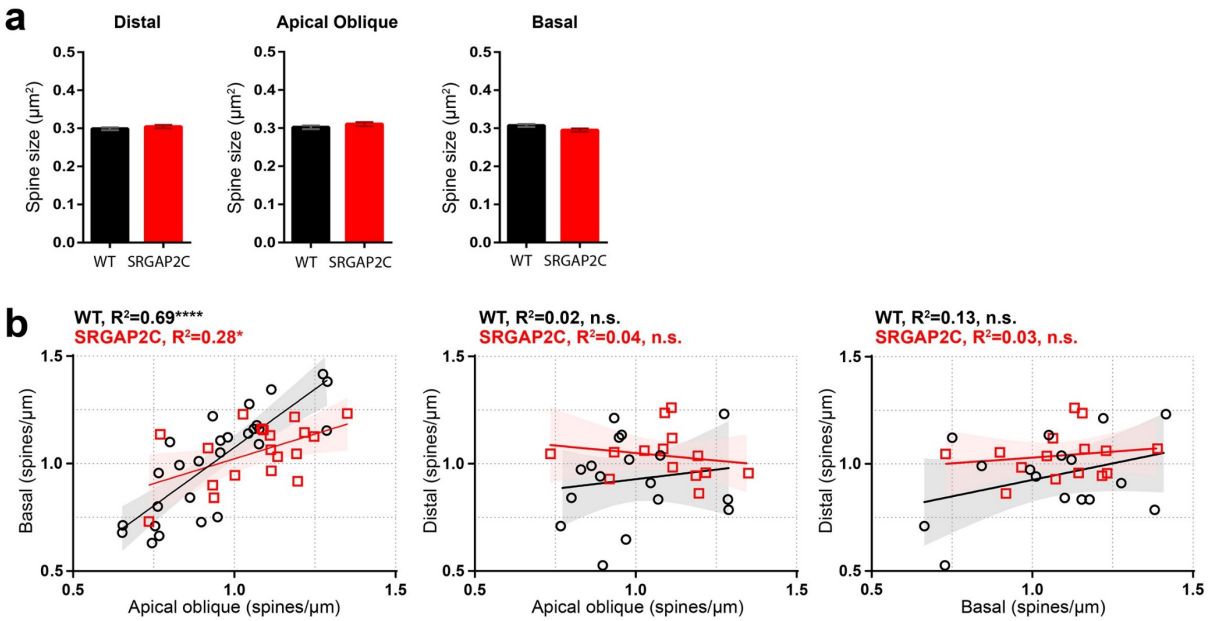

Extended Data Fig. 7. Spine size and correlation of spine density across dendritic domains is altered in SRGAP2C mice

a, Spine size is not altered in adult SRGAP2C expressing layer 2/3 cortical pyramidal neurons. (distal: *n* = 1273 spines for WT and *n* = 1083 spines for SRGAP2C, apical oblique: *n* = 2401 spines for WT and *n* = 1650 spines for SRGAP2C, basal: *n* = 2286 spines for WT and *n* = 1448 spines for SRGAP2C). Bar graph plotted as mean ± s.e.m. **b**, Correlation analysis of spine density between apical oblique, basal, and distal dendritic domains. Significant correlation was found for spine density between apical oblique and basal dendritic domains. (Pearson's correlation coefficient $r = 0.83$, slope = 1.09, $P < 1 \times 10^{-4}$). In SRGAP2C mice this correlation and the slope was reduced (Pearson's correlation coefficient $r = 0.52$, slope = 0.46, $P = 2.1 \times 10^{-2}$). Analysis was done on a subset of neurons for which we had spine density information for at least two separate dendritic domains (apical oblique vs basal: *n* = 27 neurons for WT and *n* = 19 neurons for SRGAP2C, apical oblique vs distal: *n* = 17 neurons for WT and *n* = 14 neurons for SRGAP2C, Basal vs distal: *n* = 16 neurons for WT and *n* = 15 neurons for SRGAP2C). ****$P < 0.0001$, *$P < 0.05$.

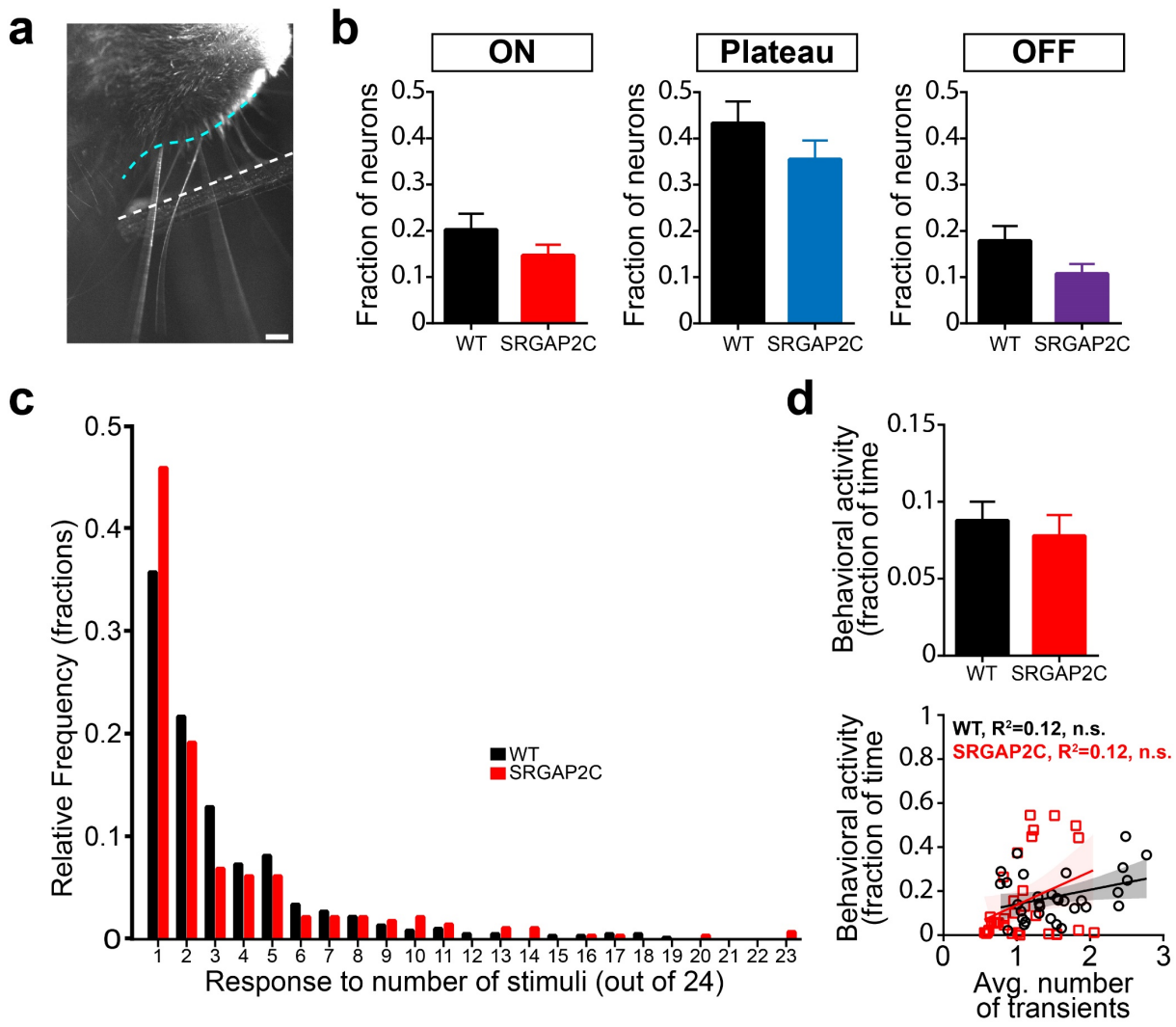

Extended Data Fig. 8. Neuronal activity in response to whisker stimuli.

a, Top-down view of placement of rod (white dashed line, 2mm away from the whisker pad) next to right whisker pad (cyan dashed line). Scale bar, 1mm. **b**, Fraction of neurons responding to onset, plateau phase, or offset of whisker stimulus. **c**, Frequency distribution of response fraction for neurons responding to either onset, plateau phase, or offset of the stimulus. **d**, Top panel: fraction of time during which behavioral activity was observed. Bottom panel: correlation between behavioral activity and average number of transients.

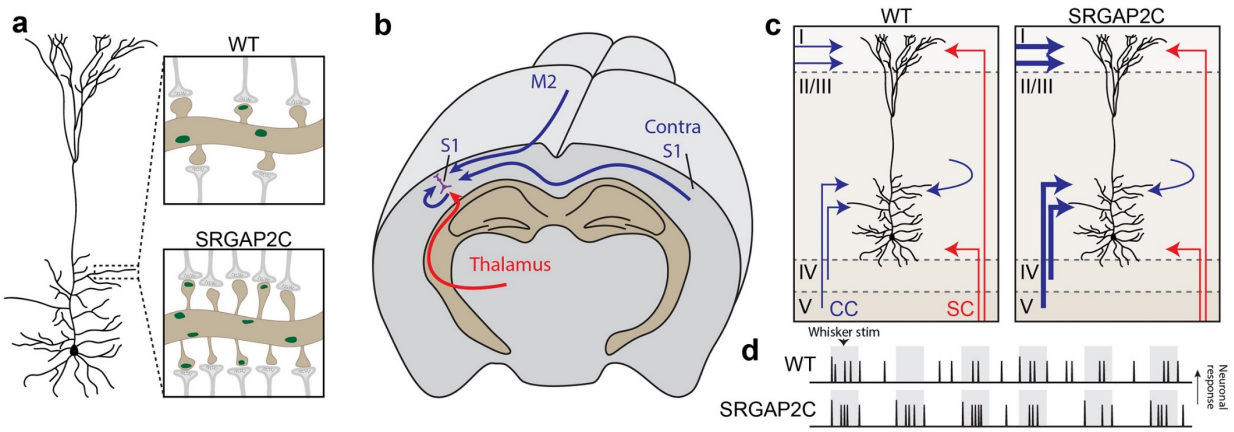

Extended Data Fig. 9. SRGAP2C-induced changes in connectivity and neuronal response properties.

Schematic summarizing main findings. **a**, SRGAP2C expression in mouse layer 2/3 cortical pyramidal neurons (PNs) increase synaptic density of both excitatory synapses (dendritic spines) and inhibitory synapses (green puncta). **b**, **c** Expression of SRGAP2C in layer 2/3 PNs in the barrel field of the primary somatosensory cortex (S1) leads to an increase in local and long-range cortico-cortical connectivity (CC, blue), without affecting subcortical inputs (SC, red). **d**, Sensory-evoked responses are more reliable and selective in SRGAP2C-expressing PNs.

Extended Data Movie 1. 3D reconstruction of a representative RABV traced brain mapped onto Allen Reference Atlas.

Movie of a representative reconstructed RABV traced brain. Reference brain was adapted from the Allen Institute. Octahedrons represent RABV traced neurons and are color coded based on their anatomical location. See text for details.